Materials Horizons

ROYAL SOCIETY OF CHEMISTRY

COMMUNICATION

View Article Online
View Journal | View Issue

Cite this: *Mater. Horiz.*, 2023, **10**, 2417

Received 20th March 2023,
Accepted 31st March 2023

DOI: 10.1039/d3mh00420a

rsc.li/materials-horizons

The effects of intercalated environmental gas molecules on carrier dynamics in WSe_2/WS_2 heterostructures†

Yanxue Zhang,‡[a] Hongsheng Liu,‡[b] Yanyan Zhao,[a] Jiaqi Lin,*[c] Yizhen Bai,[b] Jijun Zhao*[ab] and Junfeng Gao*[ab]

Effective tuning of carrier dynamics in two-dimensional (2D) materials is significant for multi-scene device applications. Using first-principles and *ab initio* nonadiabatic molecular dynamics calculations, the kinetics of O_2, H_2O, and N_2 intercalation into 2D WSe_2/WS_2 van der Waals heterostructures and its effect on carrier dynamics have been comprehensively explored. It is found that the O_2 molecule prefers to dissociate into atomic O atoms spontaneously after intercalation of WSe_2/WS_2 heterostructures, whereas H_2O and N_2 molecules remain intact. O_2 intercalation significantly speeds up the electron separation process, while H_2O intercalation largely speeds up the hole separation process. The lifetime of excited carriers can be prolonged by O_2 or H_2O or N_2 intercalations. These intriguing phenomena can be attributed to the effect of interlayer coupling, and the underlying physical mechanism for tuning the carrier dynamics is fully discussed. Our results provide useful guidance for the experimental design of 2D heterostructures for optoelectronic applications in photocatalysts and solar energy cells.

New concepts

The 2D van der Waals transition metal dichalcogenide (TMD) heterostructures with type-II band alignment are promising for applications in optoelectronics. During the process of fabrication and transfer, gas molecules can be easily intercalated into the interlayer space of the heterostructure. However, knowledge about the effect of gas molecule intercalation on the photo-generated carrier dynamics of heterostructures is still lacking. Herein, we systematically explore the carrier dynamics of environmental gas molecule ($O_2/H_2O/N_2$) intercalation in WSe_2/WS_2 heterostructure using the advanced TDDFT method. Intercalation of either O_2 or H_2O or N_2 reduces the band gap of pristine WSe_2/WS_2 heterostructure. The type-II band alignment is robust after $O_2/H_2O/N_2$ intercalation. Importantly, intercalation suppresses the electron–hole recombination and thus prolongs the lifetime of excited carriers. Our exploration provides new ideas for using gas molecule intercalation to modulate the carrier dynamics of van der Waals TMD heterojunctions.

Introduction

The van der Waals (vdW) heterostructures constructed by vertically stacking different 2D materials bring new physical properties and enrich the family of 2D materials.[1–5] Compared with pristine 2D materials, vdW heterostructures show unique electronic and optical properties that can be used for transistors and photodetectors.[6–9] Recent theoretical and experimental studies have demonstrated the feasibility of band alignment engineering by stacking different 2D monolayer materials.[7,10–13] Indeed, ultrafast electron transfer in transition metal dichalcogenide (TMD) vdW heterostructures, such as $MoS_2/MoSe_2$, $WSe_2/MoSe_2$, and MoS_2/WS_2, has been confirmed.[14–19] In particular, the unique type-II band alignment promotes the interlayer exciton formation[20–22] and effectively separates the photogenerated electron–hole pairs, which holds promise in the fields of photocatalysts and solar cells.[23–26] Due to the robust type-II band alignment, WSe_2/WS_2 vdW heterostructure has attracted considerable attention.[27–38]

In vertical heterostructures, the vdW gap between monolayer components offers space for the intercalation of ions and molecules, thereby giving rise to new opportunities for property modulation. It has been evidenced that ion intercalation into TMD heterostructures has a significant impact on the chemical and physical properties and leads to broad applications in energy storage.[39–41] For example, Liang *et al.* proposed a strategy

[a] *State Key Laboratory of Structural Analysis, Optimization and CAE Software for Industrial Equipment (Dalian University of Technology), Ministry of Education, Dalian, 116024, China. E-mail: gaojf@dlut.edu.cn, zhaojj@dlut.edu.cn*
[b] *Key laboratory of Materials Modification by Laser, Ion and Electron Beams (Dalian University of Technology), Ministry of Education, Dalian, 116024, China*
[c] *The School of Bioengineering, Dalian University of Technology, Dalian, 116024, China. E-mail: jqlin@dlut.edu.cn*

† Electronic supplementary information (ESI) available: Computational methods, band structures, $O_2/H_2O/N_2$ intercalation model, bond lengths, bond angle and energy comparison, charge density difference, time-dependent energy state evolution, electron and hole population, phonon spectra, average NAC values, band gap distribution, RMSD. See DOI: https://doi.org/10.1039/d3mh00420a

‡ These authors contributed equally to the work.

of water and oxygen incorporation to tune the interlayer space and hydrophilicity of MoS_2 and achieved high Zn^{2+} storage capacity.[42] Zhang *et al.* significantly enhanced the photoluminescence and photocurrent of TMD materials through tailoring the interlayer interaction by soft plasma intercalation.[43] Recently, Qian *et al.* successfully synthesized a chiral molecule-intercalated TaS_2 or TiS_2 superlattice, which provides a platform for studying the chiral-induced spin selectivity effect.[44] Beyond, Liu *et al.* successfully synthesized Cu atom intercalated NbS_2, which improves the electrical conductivity and suppresses the transition temperature and volume fraction of the superconductor.[45]

In the laboratory, the vdW heterostructures can be synthesized by mechanically-assembled stacking, chemical vapor deposition, and physical epitaxy method.[46,47] In the process of fabrication and transfer, intercalation of the ambient gas molecules into the interlayer space is inevitable.[48] On the one hand, similar to the effects of ion intercalation, molecule intercalation could also have a significant influence on the electronic and optoelectronic properties of TMD heterostructures,[40,43] which should be carefully considered. On the other hand, intercalation of ambient gas molecules could be an easy but powerful way to modify the structure, stacking mode, and related properties of 2D TMD materials.[49] Small molecule (such as O_2, H_2O) intercalation in interlayer space has been extensively observed experimentally.[50–57] To our best knowledge, however, the intercalation behavior of ambient gas molecules such as O_2, H_2O, and N_2 and their influence on the carrier dynamics of vdW heterostructures has been rarely studied.

In this study, taking the WSe_2/WS_2 vdW heterostructure as an example, the intercalation effect of O_2, H_2O, and N_2 molecules on the carrier dynamic was carefully investigated by using the state-of-the-art Hefei-NAMD[58] code (more details in ESI†), which can well describe the dynamic behavior of excited state carriers at time, space, momentum, and energy scales.[59–64] We find that O_2, H_2O, and N_2 intercalation reduces the band gap of the system but would not change the type-II band alignment of the pristine heterostructure. Interestingly, O_2 intercalation, H_2O intercalation, and N_2 intercalation can effectively modulate carrier dynamics in WSe_2/WS_2 vdW heterostructures. Our work provides a new perspective into the carrier dynamics modulation in WSe_2/WS_2 vdW heterostructures by molecule intercalation.

Results and discussions

The equilibrium lattice constants of monolayer WS_2 and WSe_2 are 3.183 Å and 3.317 Å, respectively, in agreement with previous theoretical results.[65–68] According to previous study, the WSe_2/WS_2 vdW heterostructure with C7 stacking is the most stable configuration.[35,37,38,65,69,70] Thus, we focus on C7 configuration in this study, while our test calculations on other geometries like T stacking demonstrate that molecule intercalation would not change the sequence of energies for the bilayer heterostructures. In order to reduce the lattice mismatch, the lattice constant of the WSe_2/WS_2 heterostructure is set to be the average value of the lattice constants of WSe_2 and WS_2. The WSe_2 layer is compressed by 2%, and the WS_2 layer is stretched by 2%. To check the strain effect on the band gap, we calculated the band structures of WSe_2 and WS_2 monolayers with different strain values, as shown in Fig. S1 (ESI†). The results show that a strain of 4% has a significant effect on the band gap. Fortunately, a strain of 2% has only a small effect on the band gap. Therefore, the deformation of both layers is a good choice to maintain the band gap, consistent with the previous theoretical work.[67,71] According to the projected density of states (DOS) in Fig. 1(e) and the orbital projected band structures in Fig. S2 (ESI†) for pristine WSe_2/WS_2 vdW heterostructure, the valence band maximum (VBM) mainly originates from WSe_2 and the conduction band minimum (CBM) mainly comes from WS_2. Therefore, WSe_2/WS_2 vdW heterostructures exhibit typical type-II band alignment, which is promising for photocatalysts and solar cells due to the easy separation of photo-generated electron–hole pairs. Using the Perdew–Burke–Ernzerhof functional (PBE) functional, the theoretical band gap of WSe_2/WS_2 vdW heterostructure is 0.81 eV, which is rather close to the previous reports (0.82 eV).[65] The band gap is largely reduced in the heterostructure compared with monolayer WS_2 (1.80 eV) and WSe_2 (1.54 eV),[66,72] as shown in Fig. S1 (ESI†).

As shown in Fig. 1(a)–(d), we build a $3 \times 3 \times 1$ orthogonal supercell for WSe_2/WS_2 vdW heterostructure and insert one O_2 or H_2O or N_2 molecule per supercell to investigate the intercalation effect. The lateral dimensions of the supercell are 9.75 Å and 16.89 Å, which are sufficiently large to avoid the intercalated molecule and its periodic replicas. Different intercalation sites for O_2 molecules were tested (see Fig. S3, ESI†). O_2 molecules are more likely adsorbed and dissociated on the WS_2 layer. Notably, O_2 intercalation did not change the stacking geometry of C7. Upon intercalation, the O_2 molecule will spontaneously dissociate. As depicted in Fig. 1(b), one S–W bond is broken, and a new W–O–S–O bond geometry is formed. The detailed bond lengths are summarized in Table S1 (ESI†). Intercalation of the O_2 molecule increases the interlayer spacing d by about 0.07 Å. (see Table S1, ESI†). Fig. S4 (ESI†) shows that the dissociation barrier of the O_2 molecule in the interlayer of the WSe_2/WS_2 heterostructure is 0.18 eV. In contrast, the O_2 molecule prefers physisorption on pristine monolayer WS_2.[72,73] Therefore, the confinement environment does activate O_2 molecules, which can be understood by analyzing the charge transfer. The charge density difference ($\Delta\rho$) was calculated as follows,

$$\Delta\rho = \rho_{\text{total}} - \rho_{WSe_2} - \rho_{WS_2} - \rho_{O_2/H_2O/N_2} \quad (1)$$

where ρ_{total}, ρ_{WSe_2}, ρ_{WS_2} and $\rho_{O_2/H_2O/N_2}$ denote the charge density of heterostructure, monolayer WSe_2, monolayer WS_2, O atoms and H_2O and N_2 molecule, respectively. After O_2 intercalation, electrons accumulate on two O atoms, and the heterostructure loses electrons. The electrons transferred from the heterostructure to the intercalated O_2 molecule promote the dissociation of the O_2 molecule. The charge density difference is plotted and shown in Fig. S5b of ESI.†

Different intercalation sites for H_2O molecules have also been tested (Fig. S6, ESI†), and the most stable configuration is

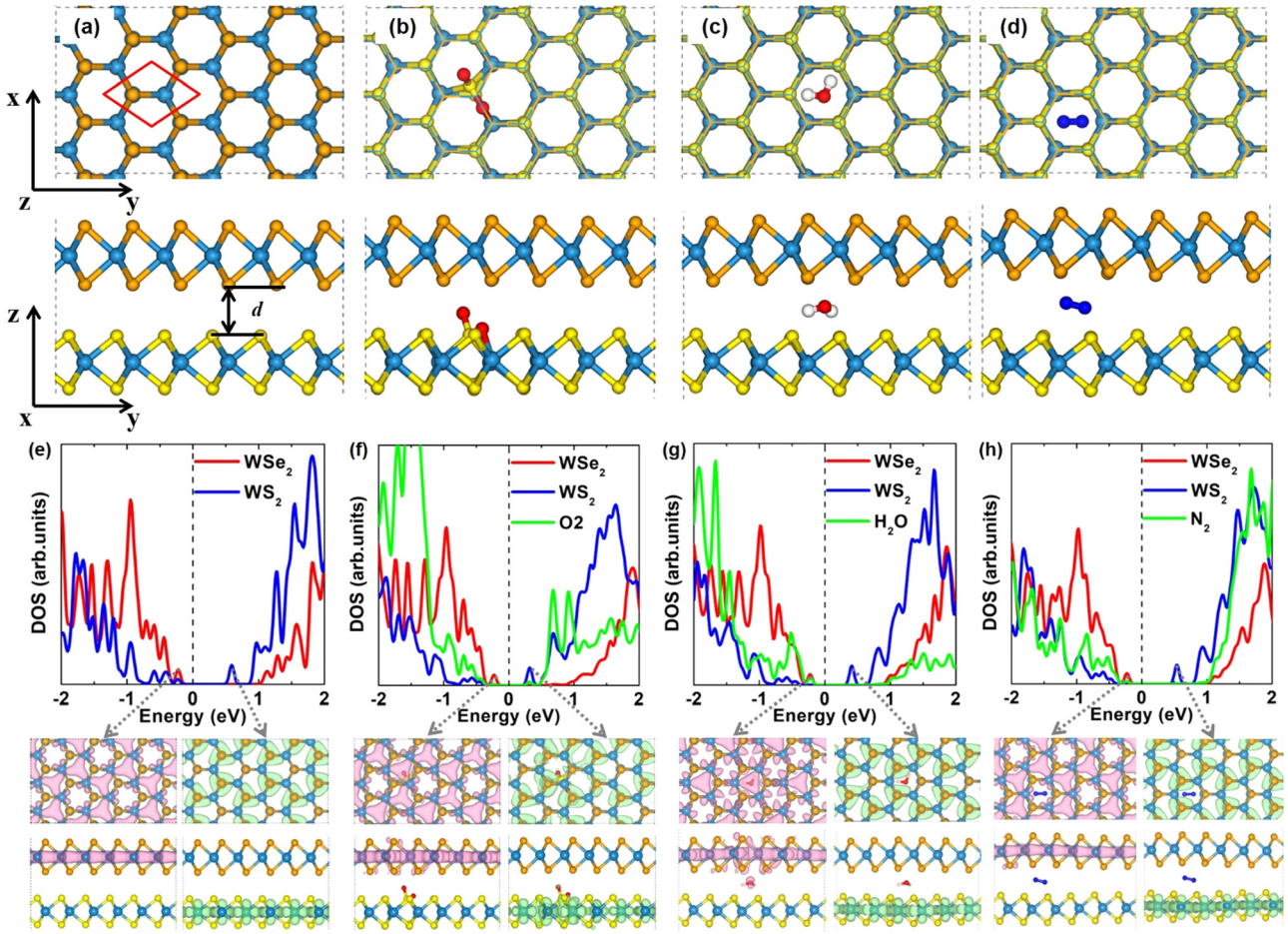

Fig. 1 Optimized structure, projected density of states (DOS), and charge density of (a), (e) pristine, (b), (f) O_2 and (c), (g) H_2O, and (d), (h) N_2 intercalated WSe_2/WS_2 vdW heterostructures. The white, red, dark blue, yellow, orange, and blue balls represent H, O, N, S, Se, and W atoms, respectively. To visualize the structure of molecules in the interlayer space, the WSe_2 layer is shown in thin-stick style in (b)–(d). The pink and green colors represent the charge density of VBM and CBM, respectively. The isosurface value is set as 0.0008 |e| $Bohr^{-3}$.

presented in Fig. 1(c). Again, the stacking pattern of C7 is not changed by H_2O intercalation. In contrast to the case of O_2 intercalation, the intercalated H_2O molecule would not dissociate. The H_2O molecule prefers to locate at the hollow site independent of initial configurations. The two H atoms of the H_2O molecule tend to be closer to the S atoms of the WS_2 layer. Intercalation of the H_2O molecule enlarges the interlayer distance by 0.13 Å. The details of the interlayer distances of H_2O intercalated heterostructures can be found in Table S2 of ESI.† Compared to the H_2O molecule in vacuum, the intercalated one has a longer O–H bond and a narrower H–O–H bond angle, indicating that the confinement environment also activates the H_2O molecule. The charge density difference (Fig. S5c, ESI†) reveals the electron transfer between the heterostructures and the H_2O molecule.

Possible intercalation sites for the N_2 molecule are examined as shown in Fig. S7 (ESI†), and the most stable configuration is shown in Fig. 1(d). N_2 molecule intercalation also did not change the stacking pattern of C7, and the N_2 molecule did not dissociate. N_2 molecule prefers to locate at the hollow site after optimization independent of initial configurations. Intercalation of the N_2 molecule increases the larger interlayer distance by about 0.32 Å. The details of the bond lengths and interlayer distances of N_2 intercalated heterostructures are shown in Table S3 of ESI.† Furthermore, the charge density difference of the N_2 intercalated heterostructure is calculated as shown in Fig. S5d (ESI†), from which we can see that the interface charge is reduced compared with the pristine heterostructure (Fig. S5a, ESI†).

It is noted that the pristine WSe_2/WS_2 heterostructure is built by deforming both layers. Whether it is the strain that causes O_2 dissociation is unclear. To examine this, the O_2, H_2O, and N_2 intercalation in an unstrained bilayer WS_2 layer with 2H stacking was investigated, as shown in Fig. S8 (ESI†).[68,74] Similar to the case of the intercalation in WSe_2/WS_2 heterostructure, in the bilayer WS_2, O_2 tends to dissociate while H_2O and N_2 remain intact. Therefore, the strain effect on the dissociation of O_2 molecules can be excluded. In experiments, small molecule intercalation in the interface of graphene and substrate has been extensively observed.[50–52,56] For example, O_2 and H_2O intercalation in the interface of graphene/Cu(111) surface leads to surface oxidation and promotes the decoupling of graphene from the substrate.[56] Besides, the surface and

catalysis are strongly influenced by a 2D cover, and the interface between adjacent 2D layers or 2D overlayers and metal substrates can be interesting 2D nanocontainers as well as 2D nanoreactors.[53] According to the above analysis, the dissociation of the O_2 molecule is expected to be the result of the space confinement effect.

According to the projected density of states (DOS) and charge densities in Fig. 1(e)–(h), intercalation of O_2 or H_2O or N_2 does not change the feature of type-II band alignment of the WSe_2/WS_2 vdW heterostructure, *i.e.*, the VBM mainly from WSe_2 and the CBM mainly from WS_2, respectively. However, molecule intercalation can prominently reduce the band gap of the system. The band gaps of O_2, H_2O, and N_2 intercalated heterostructures are 0.54 eV, 0.63 eV, and 0.76 eV, respectively. As shown in Fig. 1(e), the VBM and CBM of pristine heterostructure are located at −0.276 eV and 0.538 eV, respectively. It can be seen in Fig. 1(f) that the decreased band gap in O_2 intercalated heterostructure is caused by the downward movement of conduction bands of the WS_2 layer (CBM: 0.304 eV) and slightly upward shift of valence bands of the WSe_2 layer (VBM: −0.233 eV) after O_2 intercalation. The downward movement of conduction bands near CBM can be used as an intermediate state of electron transfer from the WSe_2 layer to the WS_2 layer and is expected to promote the fast charge transfer from the WSe_2 layer to the WS_2 layer. To clearly see the energy positions of O-related defect levels in the electronic structures, the projected density of states of molecules in Fig. 1 is magnified by a factor of one hundred. From Fig. 1(f), we can see that O defect levels do not contribute to the VBM and CBM. Impurity energy levels induced by O_2 dissociation locate between the CBM of the WS_2 layer and the CBM of the WSe_2 layer in the conduction band region. Therefore, during the electron transfer process, the donor state is not changed. O defect levels can be regarded as intermediate states of electron transfer from the WSe_2 layer to the WS_2 layer. In the valence band area, the valence bands of the WS_2 layer are shifted down, the coupling of the WSe_2 layer and WS_2 layer is reduced after O_2 intercalation, and a small part of O impurity energy levels exist between the VBM of the WS_2 layer and VBM of WSe_2 layer. As shown in Fig. 1(g), the reduced band gap in H_2O intercalated heterostructure is due to the shift down of the conduction bands of the WS_2 layer (CBM: 0.407 eV) and mildly upward shift of VBM of the WSe_2 layer (VBM: −0.223 eV). The conduction bands near the CBM of the WS_2 layer are moving down, which can also serve as an intermediate state of electron transfer between the WSe_2 and WS_2 layers. In the valence band area, the valence bands of the WS_2 layer are shifted down and the coupling of WSe_2 and WS_2 is reduced, similar to O_2 intercalation. To clearly show the effect of the H_2O molecule, the project DOS of the H_2O molecule is magnified by 100 times in Fig. 1(g). From this, we can see that the projected DOS of the H_2O molecule located between the VBM of the WS_2 layer and VBM of the WSe_2 layer, which can be an intermediated state between the WS_2 layer and the WSe_2 layer and promote hole transfer. The charge density of VBM is composed of H_2O molecule and WSe_2 layer, indicating that the highest occupied molecular orbital of the H_2O molecule is elevated and can be a hole acceptor. As shown in Fig. 1(h), in the conduction band area, N_2 intercalation also induced the conduction bands of the WS_2 layer (CBM: 0.513 eV) and VBM of the WSe_2 layer (VBM: −0.248 eV) to move down and up slightly. The conduction band near CBM is also moved downward, which can be as an intermediate state between the CBM of the WSe_2 layer and the CBM of WS_2 layer and promote electron transfer. In the VBM, the coupling of WSe_2 and WS_2 is also reduced. The projected DOS of the N_2 molecule is also magnified 100 times for clarity, which has less effect on the VBM than the H_2O molecule.

The large supercell-induced band folding containing seven irreducible K points is shown in Fig. S9 (ESI†). In order to clearly show the changes in band edge position, the band structures of pristine, O_2 intercalated, H_2O intercalated, and N_2 intercalated WSe_2/WS_2 heterostructures are unfolded as shown in Fig. S10b, d, f and h (ESI†), respectively.[75] Compared with the pristine heterostructure, the CBM band offset ΔE_C between the CBM at K of WS_2 (CB-WS_2@K) state and the CBM at K of WSe_2 (CB-WSe_2@K) state increased after molecule intercalation. The VBM at Γ of WSe_2 (VB-WSe_2@Γ) state moved down after molecule intercalation. The VBM at K of WS_2 (VB-WS_2@K) state also shifted down. Correspondingly, the VBM band offset ΔE_V between the VB-WS_2@K state and the VB-WSe_2@K state increased after molecule intercalation. The ΔE_C and ΔE_V of pristine, O_2 intercalated, H_2O intercalated, and N_2 intercalated heterostructures are summarized in Table S4 (ESI†).

As illustrated in Fig. 2(a), we focus on three processes about carrier dynamic behavior of the heterostructures: (I) transfer of photo-generated electrons from WSe_2 to WS_2, (II) transfer of photo-generated holes from WS_2 to WSe_2, (III) recombination of the photo-generated electrons and holes.

The time-dependent electron localization behavior of process (I) for pristine, O_2 intercalated, H_2O intercalated, and N_2 intercalated vdW heterostructures at 300 K has been carefully investigated. (for details, see Fig. S11a–d of ESI†). For pristine heterostructure, the initial electron distribution on the WSe_2 and WS_2 layers is 29% and 71%, respectively. After 12 fs, the spatial electron population on the WSe_2 layer decreases to 11%. Our finding agrees well with a previous theoretical study, which suggested ultrafast electron transfer from the WSe_2 layer to the WS_2 layer. In addition, recent experimental transient absorption spectroscopy has verified the ultrafast electron transfer from WSe_2 to WS_2 (∼40 fs).[65,76] In this process, the adiabatic (AD) mechanism makes the main contribution, indicating that the process is sensitive to phonon excitation. We will discuss the dominant phonon modes in the charge transfer process later. For O_2 intercalated heterostructures, the initial electron population on the WSe_2 layer is 39%. After 18 fs, the electron population on WSe_2 decreases to 19%. At 463 fs, the electron population on the WSe_2 layer completely diminishes to 0%. In this process, both AD and nonadiabatic (NA) mechanisms contribute to ultrafast electron transfer. The NA mechanism is related to direct charge hopping. For H_2O intercalated heterostructures, the initial electron distribution on the WSe_2 layer is 34%. After 18 fs, the electron population on WSe_2 decreased to 22%. At 1 ps, the electron

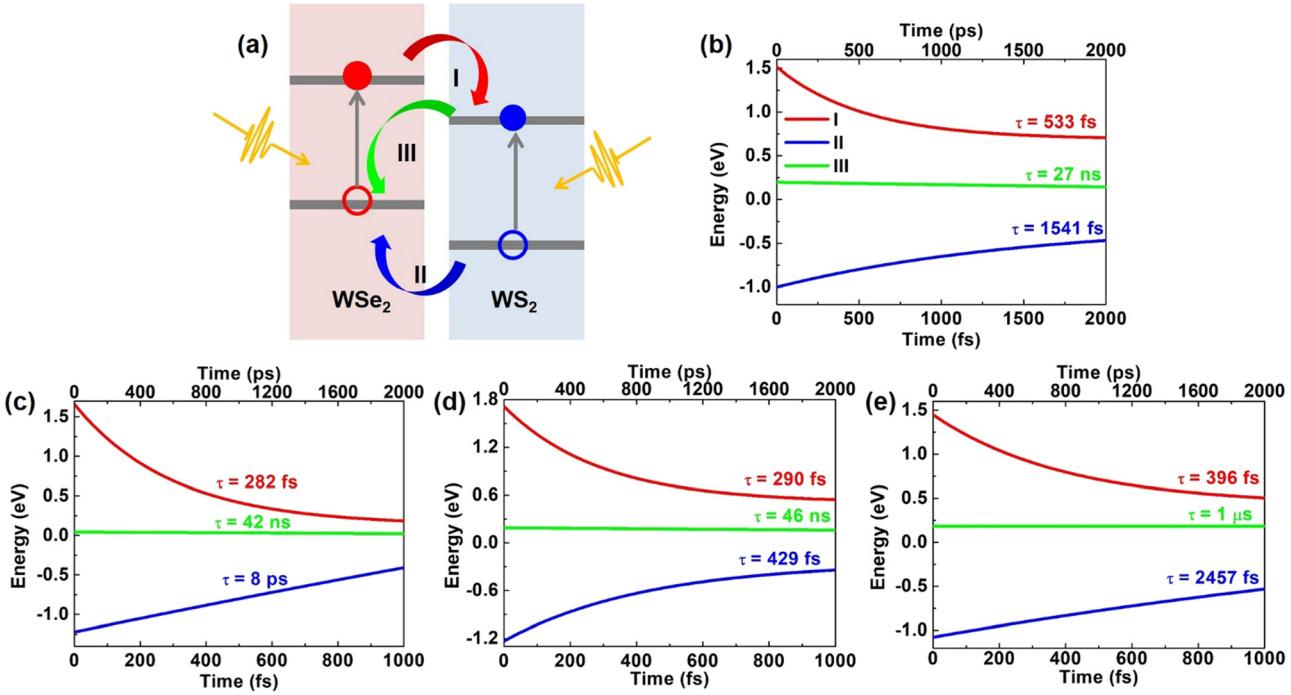

Fig. 2 (a) Schematic plots of (I) electron transfer, (II) hole transfer, and (III) electron and hole recombination processes. (b–e) show the fitting curves of time-dependent carrier energy change of three processes in (a) for pristine, O_2 intercalated, H_2O intercalated, and N_2 intercalated WSe_2/WSe_2 vdW heterostructures.

population on the WSe_2 layer decreases to 2%. In this process, the AD mechanism plays a key role. For the N_2 intercalated heterostructure, the initial electron distribution on the WSe_2 layer is 70%. After 18 fs, the electron population on WSe_2 decreased to 21%. AD mechanism dominates the fast charge transfer. Then, the electron population on the WSe_2 layer decreased and converged to 2% within 1 ps. In this process, AD and NA mechanism plays a key role. By fitting the average electron energy with exponential decay function $[A \times \exp(-t/\tau)]$, the electron transfer time for pristine, O_2 intercalated, H_2O intercalated, and N_2 intercalated heterostructures is 533 fs, 282 fs, 290 fs, and 396 fs, respectively, as shown in Fig. 2(b)–(e) (red lines). Therefore, O_2, H_2O, and N_2 intercalation can speed up the intervalley electron transfer process effectively. Details of the time-dependent electron energy profile of process (I) are shown in Fig. S11e–h (ESI†). The electron transfer pathway in momentum spaces is CB-WSe_2@K → CB-WS_2@3 → CB-WS_2@K state for pristine, O_2 intercalated, H_2O intercalated, and N_2 intercalated heterostructures.

For pristine heterostructure, the initial hole distribution on the WS_2 layer is 94%. Then, holes migrate from the WS_2 layer to the WSe_2 layer quickly. Within 40 fs, the hole population on the WS_2 layer decreases to 57%. Subsequently, at 1 ps, the hole in the WSe_2 layer gradually increases and converges to 76%. From Fig. S12e (ESI†), we can see that within 2 ps, the hole transfer pathway in momentum spaces is VB-WS_2@K → VB-WSe_2@5 → VB-WSe_2@K state. The average hole energy reached the VB-WSe_2@5 state within 1 ps. For O_2 intercalated heterostructures, the initial hole distribution on the WS_2 layer is 97%. After 25 fs, the hole population on the WS_2 layer decreases to 76%. At 73 fs, the hole population on the WS_2 layer decreases to 57%. In this process, the AD mechanism dominates. Subsequently, there is a slow hole transfer until 1 ps, where the hole population on the WSe_2 layer converges to 74%. In this process, both AD and NA mechanisms take effect. As shown in Fig. S12f (ESI†), the hole transfer pathway in momentum spaces is VB-WS_2@K → VB-WSe_2@Γ → VB-WSe_2@K state and the average hole energy reached the VB-WSe_2@Γ state within 1 ps. For H_2O intercalated heterostructures, the initial hole population on the WS_2 layer is 90%. After 18 fs, the hole population on the WS_2 layer decreases to 52%. In this process, the AD mechanism dominates. Then, the hole population on the WSe_2 layer slowly increased and converged to 74%. In this process, AD and NA mechanisms together promote hole transfer. As shown in Fig. S12g (ESI†), the hole transfer pathway in momentum spaces is VB-WS_2@K → VB-WSe_2@Γ → VB-WSe_2@K state and the average hole energy approaches the VB-WSe_2@K state within 1 ps. For N_2 intercalated heterostructures, the initial hole population on the WS_2 layer is 98%. The hole from the WS_2 layer transfers to the WSe_2 layer, and the hole population on the WS_2 layer decreases to 39% within 60 fs. AD mechanism contributes to the fast hole transfer. Then, the hole localization on the WS_2 layer oscillated until 230 fs. In this process, the AD mechanism makes the main contribution. Subsequently, the hole population on the WSe_2 layer slowly increased and converged to 66%. In this process, AD and NA mechanisms together promote hole transfer. As shown in Fig. S12h (ESI†), the hole transfer pathway in momentum spaces is VB-WS_2@K → VB-WSe_2@Γ → VB-WSe_2@K state and the average hole energy approaches the VB-WSe_2@Γ state within

1 ps. Details of the time-dependent hole localization of process (II) are given in Fig. S12a–d (ESI†). By fitting the average hole energy with an exponential decay function $[A \times \exp(-t/\tau)]$, we derive the hole transfer time as 1541 fs, 8062 fs, 429 fs, and 2457 fs for pristine, O_2 intercalated, H_2O intercalated and N_2 intercalated heterostructures, respectively, as shown in Fig. 2(b)–(e) (blue lines). Therefore, H_2O intercalation can promote ultrafast hole transfer from the VB-WS_2@K state to the VB-WSe_2@K state, while O_2 and N_2 intercalation cannot promote hole transfer. Details of the time-dependent hole energy of process (II) are shown in Fig. S12e–h (ESI†).

To investigate the electron–hole recombination, *i.e.*, the process (III) in Fig. 2(a), the time-dependent electron populations on the VBM of heterostructures have also been calculated for pristine, O_2 intercalated, H_2O intercalated, and N_2 intercalated heterostructures at 300 K. (details in Fig. S13a–d, ESI†). The initial electron population on the WSe_2 layer (VBM of the heterostructures) is 0%. For pristine heterostructure, after 2 ns, the electron population on the VBM rises to 7.6%. For O_2 intercalated heterostructures, after 2 ns, the electron population on the VBM grows to 4.9%. For the case of H_2O intercalation, after 2 ns, the electron population on the VBM rises to 4.5%. For the N_2 intercalated heterostructure, the electron population on the VBM is only 0.2% after 2 ns. By fitting the population of the electron with exponential decay: $\exp(-t/\tau) \approx 1 - t/\tau$, the electron–hole recombination time is calculated to be 27 ns, 42 ns, 46 ns, and 1 μs for pristine, O_2 intercalated, H_2O intercalated, and N_2 intercalated heterostructures, respectively, as shown in Fig. 2(b)–(e) (green lines). Therefore, molecular intercalation can effectively slow down the recombination. In the process of recombination, the NA mechanism dominates because there is no crossing between the donor state and the acceptor state.

Furthermore, we consider the effect of temperature on the carrier dynamics by performing NAMD simulations at 78 K. Our results show that for both pristine and molecule intercalated heterostructures, the decrease in temperature slightly slows down the electron transfer process but greatly slows down the hole transfer process and the recombination process. The detailed discussion can be found in the ESI† (Fig. S11–S19).

The time dependent energy level evolution of pristine, O_2 intercalated, H_2O intercalated, and N_2 intercalated heterostructures at 300 K is shown in Fig. 3(a)–(d), respectively. From this, we can see that the donor state (CB-WSe_2@K) is strongly orbital hybridized and mixed with the intermediate state during the electron transfer process. These hybrid states confirm that the AD mechanism dominates the fast electron transfer process. Especially, the CBM + 3 level and CBM + 4 level cross in intercalated heterostructures, which promotes fast electron transfer. O_2 intercalation introduces a large number of intermediate states, which further promotes the rapid transfer of electrons. In the hole transfer process, the hybrid VBM-2 level in pristine heterostructure becomes flat, localized, and gapped with VBM-1 level and VBM-3 level after O_2 intercalation, which suppresses the hole transfer. Similarly, the VBM-2 level is gapped with the VBM-1 level in N_2 intercalated heterostructure, which inhibits the hole transfer. For H_2O intercalated heterostructure, the donor state (VB-WS_2@K) is mixed with the intermediate states, which promotes rapid hole transfer.

Electron–phonon coupling during charge transfer can be obtained from the Fourier transform of the time-dependent energy level evolution. The electron–phonon coupling during charge transfer in pristine, O_2 intercalated, H_2O intercalated, and N_2 intercalated heterostructures at 300 K and 78 K is shown in Fig. 3(e)–(l) and Fig. S14(e)–(l) (ESI†), respectively. First, we

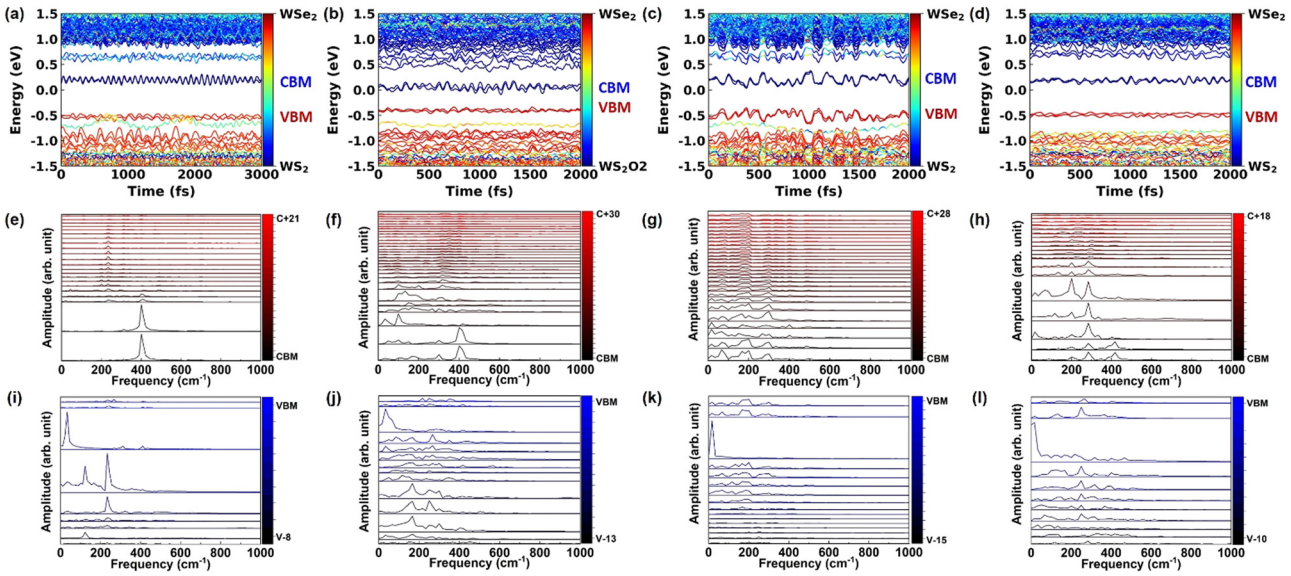

Fig. 3 The time-dependent energy evolution at Γ point of (a) pristine, (b) O_2 intercalated, (c) H_2O intercalated, and (d) N_2 intercalated heterostructures at 300 K, respectively. The color bar in (a)–(d) represents the contribution from WSe_2 layer (red part) and WS_2 layer (blue part), respectively. Fourier transforms of the donor and relevant acceptor energy states during the process of electron transfer and hole transfer in (e), (i) pristine, (f), (j) O_2 intercalated, (g), (k) H_2O intercalated, and (h), (l) N_2 intercalated WSe_2/WS_2 vdW heterostructures at 300 K, respectively. The color bar in (e)–(l) represent the band number.

discuss the phonon coupling in the pristine heterostructure. In the electron transfer process, the donor state (CBM + 21), intermediate states (CBM + 1–CBM + 20), and acceptor state (CBM) mainly couple with phonons located at 200 cm^{-1}, 233 cm^{-1}, and 400 cm^{-1} (Fig. 3(e)). In the hole transfer process, the donor state (VBM-8), intermediate state (VBM-7–VBM-1), and acceptor state (VBM) mainly couples with phonons located at 33 cm^{-1}, 122 cm^{-1}, 178 cm^{-1}, 233 cm^{-1}, 267 cm^{-1}, and 411 cm^{-1} (Fig. 3(i)). Compared with the pristine heterostructure, molecule intercalation induces many low-frequency phonon modes participating in the electron and hole transfer process, as shown in Fig. 3(f)–(h) and (j)–(l), respectively. The phonon spectra[77] of pristine, O_2 intercalated, H_2O intercalated, and N_2 intercalated WSe_2/WS_2 heterostructures are shown in Fig. S15a–d (ESI†). It can be seen that molecule intercalation induces high-frequency phonons, but phonons with a frequency larger than 1000 cm^{-1} do not participate in band edge coupling, as shown in Fig. 3(e)–(l) and Fig. S14e–l (ESI†).

Furthermore, we investigate the origin of different carrier dynamic behavior in pristine and intercalated WSe_2/WS_2 vdW heterostructures. The transfer probability of charge carriers is determined by the value of nonadiabatic coupling (NAC), which is described as:[78,79]

$$d_{jk} = \left\langle \varphi_j \left| \frac{\partial}{\partial t} \right| \varphi_k \right\rangle = \frac{\left\langle \varphi_j | \nabla_R H | \varphi_k \right\rangle}{\varepsilon_k - \varepsilon_j} \dot{R} \qquad (2)$$

Here, ε_k and ε_j are the eigenvalues of the electronic states k and j, $\langle \varphi_j | \nabla_R H | \varphi_k \rangle$ is the electron–phonon coupling element, $\dot{R}$ is the velocity of nuclear motion. According to eqn (2), a larger NAC value would promote faster charge transfer. The averaged NAC values between electronic states around the VBM and CBM for pristine and intercalated heterostructures are presented in Fig. 4.

In the process of electron transfer (process (I) in Fig. 2(a)), the averaged NAC values between different electronic states for pristine, O_2 intercalated, H_2O intercalated, and N_2 intercalated heterostructures are plotted in Fig. 4(a)–(d). In Fig. 4, each square represents the average NAC value between two different orbitals. The average NAC value is indicated by the color of the square. The color ruler is shown on the right. The darker the color, the higher the NAC value. The NAC value for two identical orbitals is zero, which is represented by white squares on the diagonal. The size of the square is meaningless. In general, according to eqn (2), the NAC value between adjacent energy levels is larger than that between distant energy levels. For example, in the pristine heterostructure, the averaged NAC value between CBM + 21 and CBM + 20 is 0.087 eV, while the NAC between CBM + 21 and CBM + 19 is 0.025 eV. Therefore, photo-excited electrons prefer to relax to the energetically adjacent states. The average NAC values between conduction states and the VBM are very small, as seen in Fig. 4(i)–(l). This accounts for the difficulty of electron–hole recombination, *i.e.*, process (III) in Fig. 2(a). The average NAC values between CBM and VBM are 1.59 × 10^{-4}, 1.53 × 10^{-4}, 1.19 × 10^{-4},

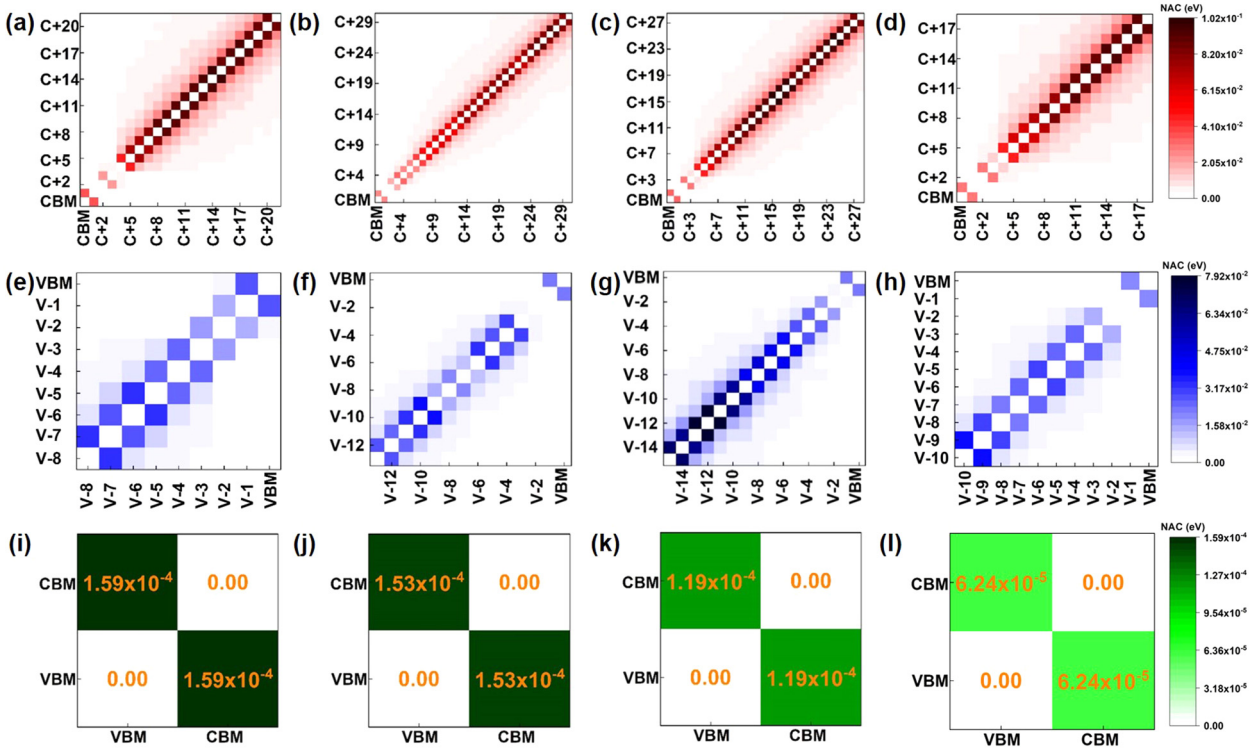

Fig. 4 The averaged NAC values between the orbitals in the process of electron transfer, hole transfer, and recombination in (a), (e), (i) pristine, (b), (f), (j) O_2 intercalated, (c), (g), (k) H_2O intercalated, and (d), (h), (l) N_2 intercalated WSe_2/WS_2 vdW heterostructures at 300 K, respectively. Here, C+1, C+2, ... means CBM+1, CBM+2,... level, respectively; V-1, V-2, ...means VBM-1, VBM-2,... energy level, respectively.

and 6.24×10^{-5} for pristine, O_2 intercalated, H_2O intercalated, and N_2 intercalated heterostructure, respectively. Therefore, the recombination of electron and hole is the most difficult in N_2 intercalated heterostructure.

The average NAC values of O_2, H_2O, and N_2 intercalated heterostructures are smaller than the pristine heterostructure, which agrees with the result of Fig. S13a–d (ESI†). Within 2 ns, pristine heterostructure has a fast recombination rate, followed by O_2 intercalation, H_2O intercalation, and N_2 intercalation. As shown in Fig. S17 (ESI†), we plot the band gap distribution during MD simulation, and the average band gap of pristine, O_2, H_2O, and N_2 intercalated heterostructures are reduced compared with the static computation. The average band gaps of pristine, H_2O, and N_2 intercalated heterostructures are 0.69 eV, 0.67 eV, and 0.64 eV, respectively. In contrast, O_2 intercalation induced a small average energy gap of 0.42 eV. A small band gap is expected to lead to large NAC values and promote fast electron–hole recombination in O_2 intercalated heterostructure. Thus, the energy level difference is not the main factor for NAC. As mentioned above, except for energy level difference, electron–phonon coupling element $\langle\varphi_j|\nabla_R H|\varphi_k\rangle$ and nuclear velocity $\dot{R}$ also play an important role in determining NAC values. The larger the energy level oscillations, the more phonons are excited and the stronger the electron phonon coupling.[58] As shown in Fig. S18a (ESI†), the relative phonon amplitude of CBM and VBM states of pristine, O_2 intercalated, H_2O intercalated, and N_2 intercalated heterostructures at 300 K are plotted. It can be seen that after molecule intercalation, the phonon amplitudes of CBM state and VBM state are reduced, indicating the smaller phonon occupation and weaker electron–phonon coupling element. Furthermore, we calculated the root mean square displacement[75,80] (RMSD) of pristine, O_2 intercalated, H_2O intercalated, and N_2 intercalated heterostructures using MD trajectories, which is defined as:

$$\mathrm{RMSD}(t) = 1/N_\alpha \sum_{i\in\alpha} \sqrt{(r_i(t) - r_i(0))^2} \qquad (3)$$

where N_α is the number of atoms including S, Se, W, $r_i(t)$ is the position of atom i at time t. The time dependent RMSD of pristine, O_2 intercalated, H_2O intercalated, and N_2 intercalated heterostructures at 300 K is shown in Fig. S19a–d (ESI†), respectively. It can be seen that O_2 intercalated, H_2O intercalated, and N_2 intercalated heterostructures have a larger RMSD than pristine heterostructure, indicating a larger nuclear velocity, which is expected to lead to larger NAC values. Thus, the reduced electron–phonon coupling element of the CBM state and VBM state is the major reason for the smaller average NAC values in molecule intercalation heterostructures.

In summary, in O_2 intercalated heterostructures, the downward shifted conduction band and the O impurity energy level induce more intermediate states between donor and acceptor, resulting in fast electron transfer from the WSe_2 layer to the WS_2 layer. In H_2O intercalated and N_2 intercalated heterostructures, the downward shifted conduction band increasing intermediate states also promote the fast intervalley electron transfer from CB-WSe_2@K state to CB-WS_2@K state at 300 K. H_2O intercalation gives rise to fast hole transfer from VB-WS_2@K state to VB-WSe_2@K state, while O_2 and N_2 intercalation do not promote hole transfer. Molecule intercalation alters the hole transfer pathway compared to pristine heterostructure. More importantly, molecule intercalation generally suppresses the recombination of electrons and holes. Overall, O_2, H_2O, and N_2 intercalation can effectively tune the carrier dynamic of WSe_2/WS_2 vdW heterostructures at a certain temperature.

Conclusions

The equilibrium structure and carrier dynamics of pristine, O_2 intercalated, H_2O intercalated, and N_2 intercalated WSe_2/WS_2 vdW heterostructures have been systematically investigated by first-principles and *ab initio* nonadiabatic molecular dynamics calculations. Our results show that at the interface of WSe_2/WS_2 vdW heterostructure, O_2 molecules will spontaneously dissociate, whereas H_2O and N_2 molecules will not. Either O_2 or H_2O or N_2 intercalation reduces the band gap of the heterostructure but will not change the type-II band alignment. At 300 K, O_2 or H_2O, or N_2 intercalation significantly speeds up the electron separation process from the CB-WSe_2@K state to the CB-WS_2@K state. At 300 K, H_2O intercalation largely accelerates the hole separation process. All three molecules suppress the recombination of electrons and hole due to the reduced electron–phonon coupling element. Our results reveal a new atomistic perspective of modulating the carrier dynamics in WSe_2/WS_2 vdW heterostructures by molecule intercalation and provide valuable guidance for the experimental design of functional 2D heterostructures.

Author contributions

Y. Zhang initialized the project, carried out the calculations, and wrote the draft. H. L., Y. Z., J. L., Y. B., J. G. and J. Z. helped with the calculation process and provided inspiring suggestions for improvement. J. G. and J. Z. supervised the whole project. All authors contributed to the discussion of the results and writing the manuscript.

Conflicts of interest

There are no conflicts to declare.

Acknowledgements

This work was supported by the National Natural Science Foundation of China (grant no. 12074053, 91961204, 12004064), the Fundamental Research Funds for the Central Universities (DUT21LAB112, DUT22ZD103), and National Foreign Expert Project (G2022127004L). The authors also acknowledge Computational support from Shanghai Supercomputer Center, DUT supercomputing center, and Tianhe supercomputer of Tianjin center.

References

1 M. Chhowalla, Z. Liu and H. Zhang, *Chem. Soc. Rev.*, 2015, **44**, 2584–2586.
2 M.-Y. Li, C.-H. Chen, Y. Shi and L.-J. Li, *Mater. Today*, 2016, **19**, 322–335.
3 Y. Liu, N. O. Weiss, X. Duan, H.-C. Cheng, Y. Huang and X. Duan, *Nat. Rev. Mater.*, 2016, **1**, 16042.
4 Y. Liu, Y. Huang and X. Duan, *Nature*, 2019, **567**, 323–333.
5 Y. Liu, S. Zhang, J. He, Z. M. Wang and Z. Liu, *Nano-Micro Lett.*, 2019, **11**, 13.
6 Q. Zeng and Z. Liu, *Adv. Energy Mater.*, 2018, **4**, 1700335.
7 R. Liu, F. Wang, L. Liu, X. He, J. Chen, Y. Li and T. Zhai, *Small Struct.*, 2020, **2**, 2000136.
8 G. Zhao, K. Rui, S. X. Dou and W. Sun, *Adv. Funct. Mater.*, 2018, **28**, 1803291.
9 S. J. Liang, B. Cheng, X. Cui and F. Miao, *Adv. Mater.*, 2020, **32**, 1903800.
10 K. Kośmider and J. Fernández-Rossier, *Phys. Rev. B*, 2013, **87**, 075451.
11 C. Zhang, C. Gong, Y. Nie, K.-A. Min, C. Liang, Y. J. Oh, H. Zhang, W. Wang, S. Hong, L. Colombo, R. M. Wallace and K. Cho, *2D Mater.*, 2016, **4**, 015026.
12 T. Kang, Z. Jin, X. Han, Y. Liu, J. You, H. Wong, H. Liu, J. Pan, Z. Liu, T. W. Tang, K. Zhang, J. Wang, J. Yu, D. Li, A. Pan, D. Pan, J. Wang, Y. Liu and Z. Luo, *Small*, 2022, **18**, 2202229.
13 C. Quan, C. Lu, C. He, X. Xu, Y. Huang, Q. Zhao and X. Xu, *Adv. Mater. Interfaces*, 2019, **6**, 1801733.
14 Q. Zheng, W. A. Saidi, Y. Xie, Z. Lan, O. V. Prezhdo, H. Petek and J. Zhao, *Nano Lett.*, 2017, **17**, 6435–6442.
15 Q. Zheng, Y. Xie, Z. Lan, O. V. Prezhdo, W. A. Saidi and J. Zhao, *Phys. Rev. B*, 2018, **97**, 205417.
16 Y. Tian, Q. Zheng and J. Zhao, *J. Phys. Chem. Lett.*, 2020, **11**, 586–590.
17 Z. Hu, X. Liu, P. L. Hernández-Martínez, S. Zhang, P. Gu, W. Du, W. Xu, H. V. Demir, H. Liu and Q. Xiong, *InfoMat*, 2022, **4**, e12290.
18 F. Ceballos, M. Z. Bellus, H.-Y. Chiu and H. Zhao, *ACS Nano*, 2014, **8**, 12717–12724.
19 J. E. Zimmermann, Y. D. Kim, J. C. Hone, U. Hofer and G. Mette, *Nanoscale Horiz.*, 2020, **5**, 1603–1609.
20 Y. Jiang, S. Chen, W. Zheng, B. Zheng and A. Pan, *Light: Sci. Appl.*, 2021, **10**, 72.
21 A. Tartakovskii, *Nat. Rev. Phys.*, 2020, **2**, 8–9.
22 N. P. Wilson, W. Yao, J. Shan and X. Xu, *Nature*, 2021, **599**, 383–392.
23 D. Unuchek, A. Ciarrocchi, A. Avsar, K. Watanabe, T. Taniguchi and A. Kis, *Nature*, 2018, **560**, 340–344.
24 C. H. Lee, G. H. Lee, A. M. van der Zande, W. Chen, Y. Li, M. Han, X. Cui, G. Arefe, C. Nuckolls, T. F. Heinz, J. Guo, J. Hone and P. Kim, *Nat. Nanotechnol.*, 2014, **9**, 676–681.
25 J. S. Ross, P. Rivera, J. Schaibley, E. Lee-Wong, H. Yu, T. Taniguchi, K. Watanabe, J. Yan, D. Mandrus, D. Cobden, W. Yao and X. Xu, *Nano Lett.*, 2017, **17**, 638–643.
26 M. M. Furchi, A. Pospischil, F. Libisch, J. Burgdorfer and T. Mueller, *Nano Lett.*, 2014, **14**, 4785–4791.
27 C. Jin, J. Kim, M. I. B. Utama, E. C. Regan, H. Kleemann, H. Cai, Y. Shen, M. J. Shinner, A. Sengupta and K. Watanabe, *Science*, 2018, **360**, 893–896.
28 E. C. Regan, D. Wang, C. Jin, M. I. Bakti Utama, B. Gao, X. Wei, S. Zhao, W. Zhao, Z. Zhang, K. Yumigeta, M. Blei, J. D. Carlstrom, K. Watanabe, T. Taniguchi, S. Tongay, M. Crommie, A. Zettl and F. Wang, *Nature*, 2020, **579**, 359–363.
29 Y. Tang, L. Li, T. Li, Y. Xu, S. Liu, K. Barmak, K. Watanabe, T. Taniguchi, A. H. MacDonald, J. Shan and K. F. Mak, *Nature*, 2020, **579**, 353–358.
30 L. Yuan, B. Zheng, J. Kunstmann, T. Brumme, A. B. Kuc, C. Ma, S. Deng, D. Blach, A. Pan and L. Huang, *Nat. Mater.*, 2020, **19**, 617–623.
31 C. Jin, Z. Tao, T. Li, Y. Xu, Y. Tang, J. Zhu, S. Liu, K. Watanabe, T. Taniguchi, J. C. Hone, L. Fu, J. Shan and K. F. Mak, *Nat. Mater.*, 2021, **20**, 940–944.
32 S. Miao, T. Wang, X. Huang, D. Chen, Z. Lian, C. Wang, M. Blei, T. Taniguchi, K. Watanabe, S. Tongay, Z. Wang, D. Xiao, Y. T. Cui and S. F. Shi, *Nat. Commun.*, 2021, **12**, 3608.
33 W. Zhao, E. C. Regan, D. Wang, C. Jin, S. Hsieh, Z. Wang, J. Wang, Z. Wang, K. Yumigeta, M. Blei, K. Watanabe, T. Taniguchi, S. Tongay, N. Y. Yao and F. Wang, *Nano Lett.*, 2021, **21**, 8910–8916.
34 H. J. Chuang, M. Phillips, K. M. McCreary, D. Wickramaratne, M. R. Rosenberger, V. P. Oleshko, N. V. Proscia, M. Lohmann, D. J. O'Hara, P. D. Cunningham, C. S. Hellberg and B. T. Jonker, *ACS Nano*, 2022, **16**, 16260–16270.
35 S. Rahman, X. Sun, Y. Zhu and Y. Lu, *ACS Nano*, 2022, **16**, 21505–21517.
36 A. Sood, J. B. Haber, J. Carlström, E. A. Peterson, E. Barre, J. D. Georgaras, A. H. Reid, X. Shen, M. E. Zajac and E. C. Regan, *Nat. Nanotechnol.*, 2023, **18**, 29–35.
37 M. Zhu, Z. Zhang, T. Zhang, D. Liu, H. Zhang, Z. Zhang, Z. Li, Y. Cheng and W. Huang, *Nano Lett.*, 2022, **22**, 4528–4534.
38 K. Wang, B. Huang, M. Tian, F. Ceballos, M. W. Lin, M. Mahjouri-Samani, A. Boulesbaa, A. A. Puretzky, C. M. Rouleau, M. Yoon, H. Zhao, K. Xiao, G. Duscher and D. B. Geohegan, *ACS Nano*, 2016, **10**, 6612–6622.
39 Y. Li, J. Zhang, Q. Chen, X. Xia and M. Chen, *Adv. Mater.*, 2021, **33**, 2100855.
40 Y. Jung, Y. Zhou and J. J. Cha, *Inorg. Chem. Front.*, 2016, **3**, 452–463.
41 A. H. Biby, B. A. Ali and N. K. Allam, *Mater. Adv.*, 2021, **2**, 5052–5056.
42 H. Liang, Z. Cao, F. Ming, W. Zhang, D. H. Anjum, Y. Cui, L. Cavallo and H. N. Alshareef, *Nano Lett.*, 2019, **19**, 3199–3206.
43 L. Zhang, H. Nan, X. Zhang, Q. Liang, A. Du, Z. Ni, X. Gu, K. K. Ostrikov and S. Xiao, *Nat. Commun.*, 2020, **11**, 5960.
44 Q. Qian, H. Ren, J. Zhou, Z. Wan, J. Zhou, X. Yan, J. Cai, P. Wang, B. Li, Z. Sofer, B. Li, X. Duan, X. Pan, Y. Huang and X. Duan, *Nature*, 2022, **606**, 902–908.

45 X.-C. Liu, *Sci. Adv.*, 2020, **6**, eaay4092.
46 K. S. Novoselov, A. Mishchenko, A. Carvalho and A. H. Castro Neto, *Science*, 2016, **353**, aac9439.
47 J. Li, J. Liang, X. Yang, X. Li, B. Zhao, B. Li and X. Duan, *Small*, 2022, **18**, 2107059.
48 S. Zhang, X. Deng, Y. Wu, Y. Wang, S. Ke, S. Zhang, K. Liu, R. Lv, Z. Li, Q. Xiong and C. Wang, *Chem. Soc. Rev.*, 2022, **51**, 4000–4022.
49 J. Wu, J. Peng, H. Sun, Y. Guo, H. Liu, C. Wu and Y. Xie, *Adv. Mater.*, 2022, **34**, 2200425.
50 P. Sutter, J. T. Sadowski and E. A. Sutter, *J. Am. Chem. Soc.*, 2010, **132**, 8175–8179.
51 E. Granas, J. Knudsen, U. A. Schröder, T. Gerber, C. Busse, M. A. Arman, K. Schulte, J. N. Andersen and T. Michely, *ACS Nano*, 2012, **6**, 9951–9963.
52 R. Larciprete, S. Ulstrup, P. Lacovig, M. Dalmiglio, M. Bianchi, F. Mazzola, L. Hornekær, F. Orlando, A. Baraldi and P. Hofmann, *ACS Nano*, 2012, **6**, 9551–9558.
53 Q. Fu and X. Bao, *Chem. Soc. Rev.*, 2017, **46**, 1842–1874.
54 C. Xia, S. Back, S. Ringe, K. Jiang, F. Chen, X. Sun, S. Siahrostami, K. Chan and H. Wang, *Nat. Catal.*, 2020, **3**, 125–134.
55 L. Zhou, X. Wang, H. J. Shin, J. Wang, R. Tai, X. Zhang, H. Fang, W. Xiao, L. Wang, C. Wang, X. Gao, J. Hu and L. Zhang, *J. Am. Chem. Soc.*, 2020, **142**, 5583–5593.
56 P. R. Kidambi, B. C. Bayer, R. Blume, Z. J. Wang, C. Baehtz, R. S. Weatherup, M. G. Willinger, R. Schloegl and S. Hofmann, *Nano Lett.*, 2013, **13**, 4769–4778.
57 J. W. Tyrrell and P. Attard, *Phys. Rev. Lett.*, 2001, **87**, 176104.
58 Q. Zheng, W. Chu, C. Zhao, L. Zhang, H. Guo, Y. Wang, X. Jiang and J. Zhao, *Wiley Interdiscip. Rev.: Comput. Mol. Sci.*, 2019, **9**, e1411.
59 S. Tan, A. Argondizzo, J. Ren, L. Liu, J. Zhao and H. Petek, *Nat. Photonics*, 2017, **11**, 806–812.
60 S. Tan, Y. Dai, S. Zhang, L. Liu, J. Zhao and H. Petek, *Phys. Rev. Lett.*, 2018, **120**, 126801.
61 L. Zhang, Q. Zheng, Y. Xie, Z. Lan, O. V. Prezhdo, W. A. Saidi and J. Zhao, *Nano Lett.*, 2018, **18**, 1592–1599.
62 W. Chu, Q. Zheng, O. V. Prezhdo and J. Zhao, *J. Am. Chem. Soc.*, 2020, **142**, 3214–3221.
63 W. Chu, Q. Zheng, O. V. Prezhdo, J. Zhao and W. A. Saidi, *Sci. Adv.*, 2020, **6**, eaaw7453.
64 X. Jiang, Q. Zheng, Z. Lan, W. A. Saidi, X. Ren and J. Zhao, *Sci. Adv.*, 2021, **7**, eabf3759.
65 H. Zeng, X. Liu, H. Zhang and X. Cheng, *Phys. Chem. Chem. Phys.*, 2021, **23**, 694–701.
66 D. Muoi, N. N. Hieu, H. T. T. Phung, H. V. Phuc, B. Amin, B. D. Hoi, N. V. Hieu, L. C. Nhan, C. V. Nguyen and P. T. T. Le, *Chem. Phys.*, 2019, **519**, 69–73.
67 K. Zollner, P. E. F. Junior and J. Fabian, *Phys. Rev. B*, 2019, **100**, 195126.
68 H.-g Kim and H. J. Choi, *Phys. Rev. B*, 2021, **103**, 085404.
69 J. Zhang, J. Wang, P. Chen, Y. Sun, S. Wu, Z. Jia, X. Lu, H. Yu, W. Chen, J. Zhu, G. Xie, R. Yang, D. Shi, X. Xu, J. Xiang, K. Liu and G. Zhang, *Adv. Mater.*, 2016, **28**, 1950–1956.
70 X. Wu, X. Wang, H. Li, Z. Zeng, B. Zheng, D. Zhang, F. Li, X. Zhu, Y. Jiang and A. Pan, *Nano Res.*, 2019, **12**, 3123–3128.
71 L. Debbichi, O. Eriksson and S. Lebègue, *Phys. Rev. B*, 2014, **89**, 205311.
72 V. Q. Bui, T. T. Pham, D. A. Le, C. M. Thi and H. M. Le, *J. Phys.: Condens. Matter*, 2015, **27**, 305005.
73 H. Liu, N. Han and J. Zhao, *RSC Adv.*, 2015, **5**, 17572–17581.
74 A. Ramasubramaniam, D. Naveh and E. Towe, *Phys. Rev. B*, 2011, **84**, 205325.
75 V. Wang, N. Xu, J.-C. Liu, G. Tang and W.-T. Geng, *Comput. Phys. Commun.*, 2021, **267**, 108033.
76 H. Zhou, C. Sun, W. Xin, Y. Li, Y. Chen and H. Zhu, *Nano Lett.*, 2022, **22**, 2547–2553.
77 A. Togo and I. Tanaka, *Scr. Mater.*, 2015, **108**, 1–5.
78 J. C. Wong, L. Li and Y. Kanai, *J. Phys. Chem. C*, 2018, **122**, 29526–29536.
79 X. Niu, Y. Li, Y. Zhang, Q. Zheng, J. Zhao and J. Wang, *J. Mater. Chem. C*, 2019, **7**, 1864–1870.
80 F. Zhang, X. Wang, W. Gao and J. Zhao, *Phys. Rev. Appl.*, 2022, **17**, 064016.

